AIAA JOURNAL
Vol. 40, No. 9, September 2002

Numerical Prediction of Fluid-Resonant Oscillation at Low Mach Number

M. Inagaki,* O. Murata,† and T. Kondoh‡
Toyota Central Research and Development Laboratories, Inc., Aichi 480-1192, Japan
and
K. Abe§
Kyushu University, Fukuoka 812-8581, Japan

A method (governing equation set and numerical procedure) suited to the numerical simulation of fluid-resonant oscillation at low Mach numbers is constructed. The new equation set has been derived under the assumption that the compressibility effect is weak. Because the derived equations are essentially the same as the incompressible Navier–Stokes equations, except for an additional term, we can apply almost the same numerical procedure developed for incompressible flow equations without difficulty. With application of a pressure-based method that treats the continuity equation as a constraint equation for pressure, the stiffness problem that arises in solving the usual compressible flow equations under low Mach number conditions has been alleviated. To verify the present method, we apply it to the flows over a three-dimensional open cavity. The results show that strong pressure fluctuations occur at specific flow velocities and that the frequency of the pressure fluctuations is locked in at the Helmholtz resonant frequency of the cavity. Thus, the present method is confirmed to have the capability of predicting fluid-resonant oscillation in low-Mach-number flows.

Nomenclature

Cp	=	pressure coefficient
c	=	speed of sound
f	=	frequency of pressure fluctuation
h_i	=	grid width in i direction
L	=	reference length
M	=	Mach number
p	=	pressure
Re	=	Reynolds number
S	=	entropy
t	=	time
U_i	=	flux velocity component in i direction
U_0	=	reference velocity
u_i	=	velocity component in i direction $(u_1, u_2, u_3) = (u, v, w)$
x_i	=	Cartesian coordinate in i direction
Δt	=	dimensionless time step
μ	=	dynamic viscosity
ρ, ρ'	=	density

Subscript

0	=	reference value

Superscript

n	=	number of time steps

I. Introduction

FLUID-RESONANT oscillation (Fig. 1) is a very interesting phenomenon, from both the physical and the engineering viewpoints. Even in low-Mach-number flows, once this phenomenon occurs, it sometimes fatally damages the device. Therefore, it is very important to predict whether fluid-resonant oscillation occurs in the operating condition of fluid machinery, as well as its magnitude if it does occur.

For example, when a vehicle runs at specific speeds with the sunroof or window open, the so-called wind-throb phenomenon occurs in the vehicle cabin. It generates a high noise level with relatively low frequency, ranging from 10 to 50 Hz. Its magnitude sometimes exceeds 130 dB, causing unacceptable discomfort to the driver and the passengers. This phenomenon is considered to be the kind of fluid-resonant oscillation categorized by Rockwell and Naudascher.[1] In that phenomenon, the periodic vortex shedding over the opening of the sunroof or window excites the resonance in the vehicle cabin, which behaves like a Helmholtz resonator. However, the wave effects of the resonance influence the vortex shedding, which means that they are strongly coupled with each other. Such a flow is observed and of interest in many areas of engineering, for example, landing-gear wells and aircraft surface-mounted instrumentation.

To predict the wind-throb phenomenon numerically, there have been attempts[2] to perform incompressible unsteady simulations. From such simulations, however, one can never predict the phenomenon by which an extremely large noise is generated at specific speeds and in a specific frequency range because the fluid-resonant oscillation can not be essentially simulated without considering the compressibility effect of the flow. Nevertheless, compressible unsteady simulation has the possibility of predicting fluid-resonant oscillation theoretically. However, it is not feasible to perform full compressible unsteady simulation of the flow around a vehicle because it results in the so-called stiffness problem in low-Mach-number flows, which creates severe convergence problems leading to inefficiency and inaccuracy.

Several approaches have been developed for simulating the aeroacoustic sound at low Mach numbers, which also results from the weak compressibility of the flow. For example, Hardin and Pope[3] introduced a scheme called *expansion about incompressible flow* (EIF). The EIF approach splits the flowfields into an incompressible part and a perturbation part. However, this approach does not allow acoustic backscatter of the perturbation part into the incompressible part and is considered not to have the capability of predicting fluid-resonant oscillation.

Thus, in this paper, we derive new basic equations suited for the simulation of fluid-resonant oscillation at low Mach numbers. The

Received 27 October 2001; revision received 28 March 2002; accepted for publication 29 March 2002. Copyright © 2002 by the American Institute of Aeronautics and Astronautics, Inc. All rights reserved. Copies of this paper may be made for personal or internal use, on condition that the copier pay the $10.00 per-copy fee to the Copyright Clearance Center, Inc., 222 Rosewood Drive, Danvers, MA 01923; include the code 0001-1452/02 $10.00 in correspondence with the CCC.

*Researcher, System Engineering and Electronics Department, Nagakute.
†Researcher, Mechanical Engineering Department, Nagakute.
‡Principal Researcher, System Engineering and Electronics Department, Nagakute.
§Associate Professor, Department of Aeronautics and Astronautics, Hakozaki, Higashi-ku.

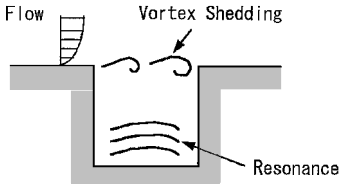

Fig. 1 Fluid-resonant oscillation.

equations are derived from the compressible Navier–Stokes equations by assuming that the compressibility effect is weak and related to the pressure deviation from the reference value. The resultant unknown variables of the equations are u, v, w, and p, so that we can apply almost the same numerical procedure developed for the incompressible flow equations. Therefore, the computational cost of the present method is comparable to that of the incompressible flow calculation. To verify the capability of the present method in simulating fluid-resonant oscillation, we apply it to flows over a three-dimensional open cavity. When the computational results are compared with the experimental data, the validity of the present method is carefully examined.

II. Methods

A. Derivation of Basic Equations

Consider compressible Navier–Stokes equations

$$\frac{\partial \tilde{\rho}}{\partial \tilde{t}} + \frac{\partial \tilde{\rho}\tilde{u}_j}{\partial \tilde{x}_j} = 0 \tag{1}$$

$$\frac{\partial \tilde{\rho}\tilde{u}_i}{\partial \tilde{t}} + \frac{\partial \tilde{\rho}\tilde{u}_j\tilde{u}_i}{\partial \tilde{x}_j} = -\frac{\partial \tilde{p}}{\partial \tilde{x}_i} + \frac{\partial \tilde{\tau}_{ij}}{\partial \tilde{x}_j} \tag{2}$$

$$\tilde{\tau}_{ij} = \tilde{\mu}\left(\frac{\partial \tilde{u}_i}{\partial \tilde{x}_j} + \frac{\partial \tilde{u}_j}{\partial \tilde{x}_i} - \frac{2}{3}\delta_{ij}\frac{\partial \tilde{u}_m}{\partial \tilde{x}_m}\right) \tag{3}$$

in which a tilde indicates dimensional value. We introduce the following dimensionless values:

$$\rho' = (\tilde{\rho} - \tilde{\rho}_0)/\tilde{\rho}_0, \qquad p = (\tilde{p} - \tilde{p}_0)\Big/\left(\tilde{\rho}_0 U_0^2\right), \qquad u_i = \tilde{u}_i/U_0$$

$$x_i = \tilde{x}_i/L, \qquad t = \tilde{t}U_0/L$$

Note that the density ρ' and the pressure p are the dimensionless values of the deviation from the reference value. By introducing these dimensionless values, we can rewrite the compressible Navier–Stokes equations as follows:

$$\frac{1}{1+\rho'}\left\{\frac{\partial \rho'}{\partial t} + u_j\frac{\partial \rho'}{\partial x_j}\right\} + \frac{\partial u_j}{\partial x_j} = 0 \tag{4}$$

$$\frac{\partial u_i}{\partial t} + \frac{\partial u_j u_i}{\partial x_j} - u_i\frac{\partial u_j}{\partial x_j} = \frac{1}{1+\rho'}\left\{-\frac{\partial p}{\partial x_i} + \frac{\partial \tau'_{ij}}{\partial x_j}\right\} \tag{5}$$

$$\tau'_{ij} = \frac{1}{Re}\left(\frac{\partial u_i}{\partial x_j} + \frac{\partial u_j}{\partial x_i} - \frac{2}{3}\delta_{ij}\frac{\partial u_m}{\partial x_m}\right) \tag{6}$$

To obtain a new equation set suited to the simulation of fluid-resonant oscillation in low-Mach-number flows, we make the following assumptions in the preceding equations:

1) For the density, the deviation from the reference value is small enough to assume $\rho' \ll 1$ because $\rho' = \mathcal{O}(M^2)$ in low-Mach-number flows. Thus, it is expressed as

$$1/(1+\rho') \approx 1 \tag{7}$$

2) When the entropy is assumed to be constant, the deviation in density can be related to the deviation in pressure as follows:

$$\frac{\mathrm{D}\rho'}{\mathrm{D}t} = M^2\frac{\mathrm{D}p}{\mathrm{D}t}, \qquad \frac{\mathrm{D}}{\mathrm{D}t} = \frac{\partial}{\partial t} + u_j\frac{\partial}{\partial x_j}$$

$$M = \frac{U_0}{c}, \qquad c^2 = \left(\frac{\partial \tilde{p}}{\partial \tilde{\rho}}\right)_S \tag{8}$$

3) Because $\partial u_m/\partial x_m = \mathcal{O}(M^2)$ as seen in Eq. (9), the effect of that term in Eq. (6) is negligibly small in comparison with the term $\partial u_i/\partial x_j + \partial u_j/\partial x_i$ in low-Mach-number flows.

These assumptions, which are considered to be reasonable in relatively high-Reynolds-number flows without a significant heat source, enable us to obtain the following new equation set:

$$M^2\left\{\frac{\partial p}{\partial t} + u_j\frac{\partial p}{\partial x_j}\right\} + \frac{\partial u_j}{\partial x_j} = 0 \tag{9}$$

$$\frac{\partial u_i}{\partial t} + \frac{\partial u_j u_i}{\partial x_j} - u_i\frac{\partial u_j}{\partial x_j} = -\frac{\partial p}{\partial x_i} + \frac{\partial \tau_{ij}}{\partial x_j} \tag{10}$$

$$\tau_{ij} = \frac{1}{Re}\left(\frac{\partial u_i}{\partial x_j} + \frac{\partial u_j}{\partial x_i}\right) \tag{11}$$

In the limit $M \to 0$, Eqs. (9–11) becomes identical to the incompressible Navier–Stokes equations. In what follows, Eqs. (9–11) are employed as the basic equations in the present study.

B. Characteristics of Present Basic Equations

It is apparent that the derived equations are essentially the same as the incompressible Navier–Stokes equations except for the additional term that expresses the deviation from the continuity condition in the incompressible flow. This term is $\mathcal{O}(M^2)$ and disappears in the incompressible flow condition. However, we maintain this term intentionally because it is expected to enable us to introduce the weak compressibility effect into the flow calculation. In other words, only this term can yield the essential difference from the incompressible flow calculation in the present study.

Next, we compare these equations with the compressible Navier–Stokes equations. The dimensionless pressure p in the present basic equations denotes the deviation from the reference value. The corresponding dimensional value $\tilde{p} - \tilde{p}_0$ is estimated as follows, if we suppose the low-Mach-number condition:

$$|\tilde{p} - \tilde{p}_0| \approx \mathcal{O}\left(\tilde{\rho}_0 U_0^2\right) \approx \mathcal{O}\left(M^2\tilde{p}_0\right) \approx \mathcal{O}(M^2\tilde{p}) \tag{12}$$

This describes that the pressure deviation in the present basic equations is M^2 times as small as the pressure $\tilde{p}$ in the compressible Navier–Stokes equations. In the same way, the dimensional value $\tilde{\rho} - \tilde{\rho}_0$ corresponding to the dimensionless density ρ', which is related to the pressure p in the present basic equations, is estimated as follows:

$$|\tilde{\rho} - \tilde{\rho}_0| \approx \mathcal{O}\left(M^2\tilde{\rho}_0\right) \approx \mathcal{O}(M^2\tilde{\rho}) \tag{13}$$

It is shown that the density deviation in the present basic equations is also M^2 times as small as the density $\tilde{\rho}$ in the compressible Navier–Stokes equations. Consequently, it is evident that the computation based on the present basic equations has a great advantage over the computation based on the compressible Navier–Stokes equations. For example, for the flow around ground vehicles where the Mach number is 0.1 at most, we can directly treat the value, which is approximately 0.01 times as small as in the computation based on the full compressible Navier–Stokes equations. This yields a great advantage in computational efficiency or computational accuracy in practical use.

C. Numerical Methods

As mentioned before, the weak compressibility effect is taken into consideration by the additional term in Eq. (9). Moreover, because the unknown variables of the present basic equations are u, v, w, and p, we can apply almost the same numerical procedure developed for the incompressible flow calculation. The most important point in solving the present basic equations is to employ a numerical method that satisfies the continuity condition in the incompressible flow calculation with high accuracy to capture the weak compressibility effect correctly because a numerical error in the continuity condition can possibly hide the compressibility effect. To satisfy this requirement, we use a collocated grid system,[4,5] which is one of the pressure-based methods used mainly for incompressible flow calculations. The collocated grid system is ascertained to satisfy

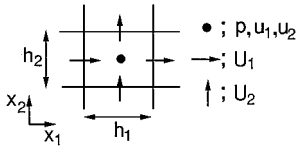

Fig. 2 Collocated grid in x_1–x_2 plane.

the continuity condition with high accuracy in incompressible flow calculations and is also confirmed to yield a nonoscillatory pressure field. We modify the collocated grid system applicable to the present basic equations as described next.

To simplify the description, we consider the rectangular grids shown in Fig. 2. The collocated grid system defines the velocity components u_i and the pressure p at the center of the cells and, at the same time, arranges the auxiliary flux velocity components U_i at the center of the cell faces. The momentum equations are solved for u_i. The continuity equation is evaluated by using U_i, which is interpolated from u_i by a special procedure.[5] The flux velocity U_i is then also used as the convection velocity in the momentum equations, that is, u_j in the second term of Eq. (10). To be consistent with this treatment, we also use U_i as u_j in the third term of Eq. (10), which disappears in the incompressible flow condition. For spatial discretization, a second-order central difference scheme is used except for the convective term of Eq. (10), to which the QUICK scheme is applied. We employ no turbulence model in this analysis. This method is often called *coherent structure capturing*,[6] which is able to capture the vortex structures with high accuracy if the size of vortex is relatively large.

The Crank–Nicolson method is employed for the time advancement of Eq. (10) except for the pressure term, for which the backward Euler method is used. A simplified marker and cell-like method is used for the coupling between the velocity and the pressure field. In this method, the continuity equation is applied to the next time step, $n+1$. The additional term in the continuity equation [the first term of Eq. (9)] is discretized as follows:

$$\left.\frac{\partial p}{\partial t}\right|^{n+1} \approx \frac{3p^{n+1} - 4p^n + p^{n-1}}{2\Delta t} \tag{14}$$

$$\left. u_j \frac{\partial p}{\partial x_j}\right|^{n+1} \approx u_j^n \frac{\delta_j p^{n+1}}{\delta_j x_j} \tag{15}$$

where $\delta_j/\delta_j x_j$ is the spatial discretization by means of the second-order central difference scheme.

The whole solution procedure is summarized as follows:

1) The intermediate velocity u_i^* is obtained by using the pressure at the previous time step n:

$$u_i^* + \frac{\Delta t}{2}\left\{\frac{\partial U_j^n u_i^*}{\partial x_j} - u_i^*\frac{\partial U_j^n}{\partial x_j} - \frac{\partial \tau_{ij}^*}{\partial x_j}\right\}$$

$$= u_i^n - \Delta t\frac{\partial p^n}{\partial x_i} - \frac{\Delta t}{2}\left\{\frac{\partial U_j^n u_i^n}{\partial x_j} - u_i^n\frac{\partial U_j^n}{\partial x_j} - \frac{\partial \tau_{ij}^n}{\partial x_j}\right\} \tag{16}$$

2) The contribution from the pressure term is subtracted from the intermediate velocity u_i^*:

$$u_i^{**} = u_i^* + \Delta t\frac{\partial p^n}{\partial x_i} \tag{17}$$

3) The intermediate flux velocity U_i^{**} at the center of the cell faces is interpolated from u_i^{**} at the center of the cells.

4) The following equation is solved for the pressure p^{n+1} at the next time step:

$$\left.\frac{\partial p}{\partial t}\right|^{n+1} + \left. u_j\frac{\partial p}{\partial x_j}\right|^{n+1} = \frac{\Delta t}{M^2}\frac{\partial^2 p^{n+1}}{\partial x_j^2} - \frac{1}{M^2}\frac{\partial U_j^{**}}{\partial x_j} \tag{18}$$

5) The velocity at the next time step is evaluated using the obtained pressure p^{n+1}:

$$u_i^{n+1} = u_i^{**} - \Delta t\frac{\partial p^{n+1}}{\partial x_i} \tag{19}$$

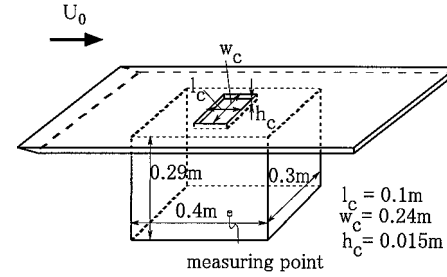

Fig. 3 Three-dimensional open cavity.

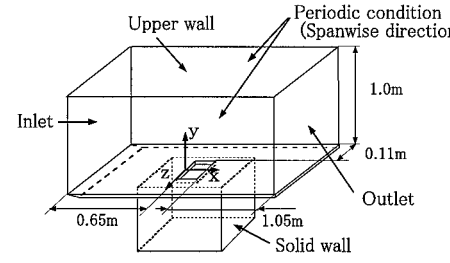

Fig. 4 Computational domain.

$$U_i^{n+1} = U_i^{**} - \Delta t\frac{\partial p^{n+1}}{\partial x_i} \tag{20}$$

By this procedure, one time step is advanced. In the limit $M \to 0$, Eq. (18) becomes identical to the well-known Poisson equation for pressure:

$$\frac{\partial^2 p^{n+1}}{\partial x_j^2} = \frac{1}{\Delta t}\frac{\partial U_j^{**}}{\partial x_j} \tag{21}$$

Because the pressure is fully implicitly solved by using Eq. (18), the stiffness problem caused from the disparity between the acoustic timescale and the convective or viscous timescale can be alleviated. For simplicity, we explained the method for rectangular grids. However, it is easily applied to curvilinear grids in the same manner, as shown by Rhie and Chow.[5]

III. Experimental and Computational Arrangements

A. Three-Dimensional Open Cavity Flows

To verify whether the present method can truly simulate fluid-resonant oscillation in low-Mach-number flows, we apply it to flows over a three-dimensional open cavity, which can be considered to simulate a vehicle cabin with a sunroof opening. The detailed shape of the open cavity is shown in Fig. 3. The experiments are performed for comparison with the computations. The experimental model of the open cavity is tested in a closed-return wind tunnel with a 0.4×0.4 m rectangular open test section, and the pressure fluctuation is measured at the center of the cavity bottom by a pressure sensor. The measurements are made for various levels of incoming flow velocity within a range of 6–54 m/s.

B. Calculation Conditions

The calculations are performed corresponding to the experimental flow conditions. To simplify the calculation conditions, we fix the Reynolds number at 2×10^5 based on the opening length l_c and the representative velocity 30 m/s and vary only the Mach number with a change in incoming flow velocity U_0. This setting of conditions is assumed to yield little difference from the measurements because the flows have little dependence on the Reynolds number, at least behind the separation at the upstream edge of the cavity opening. In these conditions, the change in the results, according to the change in the incoming flow velocity, is caused only by the additional term in Eq. (9). The speed of sound is set at 343 m/s.

Figure 4 shows the computational domain. The boundary conditions are specified as follows: 1) inlet, uniform flow ($u=1$, $v=0$, $w=0$, $p=0$); 2) outlet, Neumann condition ($\partial u_i/\partial x = 0$); 3) solid wall, artificial wall condition; 4) upper wall, slip condition ($v=0$,

$\partial u_i/\partial y = 0$); and 5) spanwise direction, periodic boundary condition. The computational domain approximately corresponds to the experimental model. The upper wall is set $10 \times l_c$ above the opening of the cavity. Because the periodic boundary condition is applied in the spanwise direction, the width in the spanwise direction somewhat differs from that in the experimental model. Note that we set the Dirichlet condition for pressure at the inlet boundary because the present basic equations involve the time-differential term of the pressure that does not appear in the incompressible Navier–Stokes equations.

The artificial wall condition used in this analysis is the following three-layer wall condition modified from the two-layer wall condition proposed by Werner and Wengle[7]:

$$u^+ = y^+ \qquad \left(y^+ \le y^+_{c1}\right) \tag{22}$$

$$u^+ = A1 y^{+B1} \qquad \left(y^+_{c1} < y^+ \le y^+_{c2}\right) \tag{23}$$

$$u^+ = A2 y^{+B2} \qquad \left(y^+_{c2} < y^+\right)$$

$$y^+_{c1} = A1^{1/(1-B1)}, \qquad y^+_{c2} = (A2/A1)^{1/(B1-B2)}$$

$$u^+ = u_p \big/ \tau_w^{\frac{1}{2}}, \qquad y^+ = Re\,\tau_w^{\frac{1}{2}} y_p, \qquad A1 = 2.7$$

$$A2 = 8.6, \qquad B1 = \tfrac{1}{2}, \qquad B2 = \tfrac{1}{7} \tag{24}$$

where u_p is the velocity component parallel to the wall, y_p is the distance from the wall, and τ_w is the wall friction stress. This type of wall condition is equivalent to the no-slip condition when the grid resolution in the direction normal to the wall surface is high enough. On the other hand, when the grid resolution is not sufficiently high, it is expected that this wall condition suppresses the decrease in the calculation accuracy. Note that, in this analysis, the grid resolution is relatively coarse only in the spanwise direction in the cavity. This grid arrangement is assumed to have little significant influence on the results. Except for the limited part, fine grids are used, where the wall condition becomes substantially identical with the no-slip wall condition.

We also employ the overlaid grid system[8] to facilitate grid generation and to reduce the computational cost. The computational domain is divided into three subgrid regions shown in Fig. 5. Grids 1 and 2 are shown in Fig. 6. The number of points of each grid is shown in Table 1. The total number of grid points is about 430,000. The minimum grid spacing is $1 \times 10^{-3} l_c$, and the dimensionless time step is set to $1 \times 10^{-3} l_c/U_0$. As the initial condition, the result of the incompressible flow calculation is used.

To check grid convergence, we also execute the calculation with finer grids for $U_0 = 22$, 30, 34, 38, and 46 m/s. The number of grid points is shown in Table 1. The number of points of grids 1 or 2 is over three times as large as that in the standard case. On the other hand, grid 3 is the same grid as in the standard case because grid 3 is considered to have smaller influence on the pressure fluctuation at the measuring point than grids 1 and 2. In this case, the minimum grid spacing is $5 \times 10^{-4} l_c$, and the dimensionless time step is set to $5 \times 10^{-4} l_c/U_0$.

Table 1 Computational grid points

Grid	Grid points
1	$76 \times 51 \times 52 = 201{,}552$
(Fine case)	$(100 \times 73 \times 86 = 627{,}800)$
2	$66 \times 50 \times 28 = 92{,}400$
(Fine case)	$(92 \times 73 \times 46 = 308{,}936)$
3	$100 \times 44 \times 30 = 132{,}000$
(Fine case)	(↑)

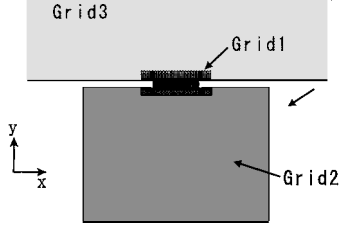

Fig. 5 Overlaid grid system.

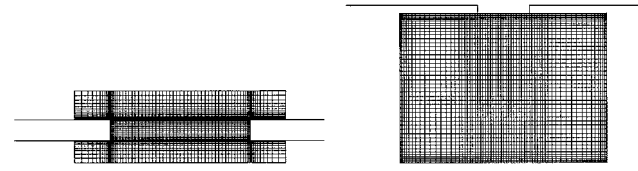

Grid 1 **Grid 2**

Fig. 6 Computational grids.

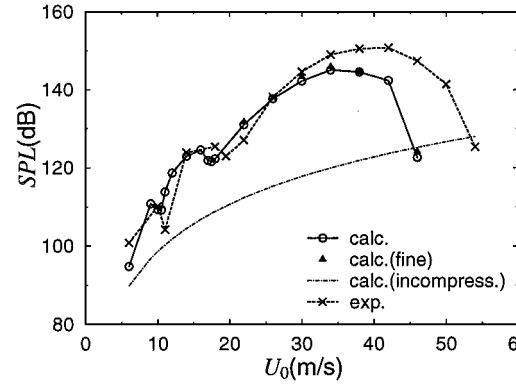

Fig. 7 Sound pressure levels.

IV. Results and Discussion

In Fig. 7, the calculated pressure fluctuations at the center of the cavity bottom are compared with the experimental data in the scale of sound pressure levels (decibels). Note that, in what follows, U_0 is defined by $U_0 = Mc$. Some peaks are clearly recognized in the plot of pressure fluctuations vs flow velocity. The computational results very successfully predict this feature. Although the flow at the center of the cavity bottom is very weak, the pressure fluctuation level at the peaks is very high. Moreover, as shown in Fig. 8, the time history of pressure under those conditions has strong periodicity and is almost a sine curve. These results suggest that the strong pressure fluctuations are probably caused by resonance. Such a fluctuation has never been detected in the results of incompressible flow calculation, which is shown by the dotted line in Fig. 7. Thus, it is thought that the peaks correspond to the occurrence of fluid-resonant oscillations. In Fig. 9, the pressure fluctuations are shown in terms of the root mean square of pressure coefficient fluctuations Cp'_{rms}, where the peaks are more clearly identified. The computational results agree well with the experimental data on the velocities at which the peaks occur. The peaks are found to occur at three velocity levels: $U_0 = 9$, 14, and 34 m/s. For the overall profile of Cp'_{rms}, the computational results agree fairly well with the experimental data.

When the results are compared quantitatively, the computational results predict the amplitude of pressure fluctuations to be lower than the experimental data in the range over 25 m/s. For example, the error of the amplitude in the case of $U_0 = 34$ m/s, where the amplitude of the pressure fluctuation takes the maximum value, is about 35%, which is about 5 dB on the scale of sound pressure levels. Using finer grids, the error is somewhat reduced. However, the improvement is not as much on the scale of sound pressure levels, which is about 0.8 dB in the case of $U_0 = 34$ m/s. This error may be caused by the numerical method employed here. The implicit scheme in the time advancement possibly provides damping of the acoustic modes. However, the property of the boundary layer approaching the opening of the cavity might have some influence on the fluctuations. Several experimental studies (for example, Sarohia[9] and Gharib[10]) have examined the relation between the property of the boundary layer and the vortex shedding under the condition of no resonance effect. Through these studies, it has been found that the property of

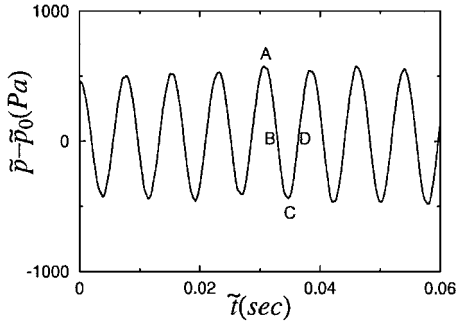

Calculation

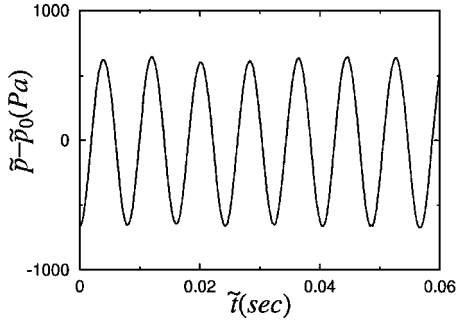

Experiment

Fig. 8 Time history of pressure for U_0 = 34 m/s.

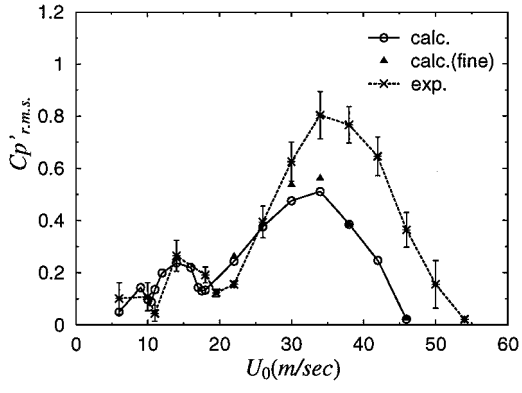

Fig. 9 Root mean square of pressure coefficient fluctuations.

the boundary layer affects the vortex shedding. Especially, the momentum thickness of the boundary layer is an important parameter. In the present computation, the boundary layer is laminar because of a uniform flow condition applied at inlet boundary, whereas it is turbulent in the experiment. In both cases, however, the boundary-layer momentum thickness is so thin compared to the length of the cavity opening that the pattern of the vortex shedding is assumed to be in a higher frequency mode or wake mode, according to the study by Gharib.[10] In a higher frequency mode, the frequency of the vortex shedding greatly differs from that of the resonance in the range over 25 m/s. In the wake mode, the vortex shedding does not have a dominant frequency. Moreover, in our study, very large pressure fluctuations, the amplitude of which is much larger than that yielded by the vortex shedding itself, are excited by coupling with the effects of the resonance. Thus, it is considered that the influence of the boundary-layer property is relatively small in the present study.

In Fig. 10, the dominant frequency of the pressure fluctuations is plotted vs U_0. With the calculation conditions applied in this analysis, it may be expected that the dominant frequency of the pressure fluctuations varies continuously in proportion to U_0. However, our results, in which the compressibility effect is taken into account, show a discontinuous change in frequency. The well-known empirical formula for estimating the vortex-shedding frequencies was presented by Rossitar[11] as follows:

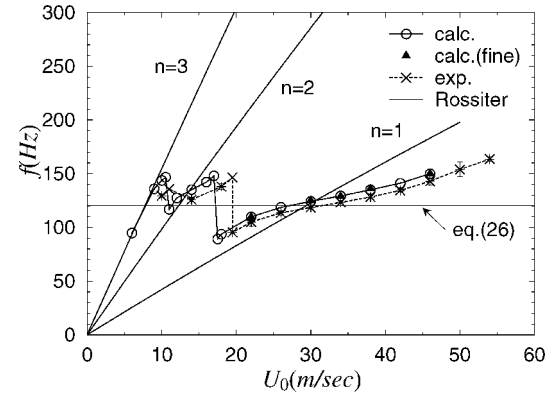

Fig. 10 Dominant frequencies of pressure fluctuations.

$$f_c = \frac{n - 0.25}{M + 1.75}\frac{U_0}{l_c} \tag{25}$$

where n is the oscillation mode number. This estimation is shown by the bold solid lines in Fig. 10, and the frequency of the Helmholtz resonance estimated by Eq. (26) is shown by the thin solid line in Fig. 10. Thus,

$$f_a = (c/2\pi)\sqrt{A\Big/\left(h_c + 0.82\sqrt{A}\right)V} \tag{26}$$

A is the area of the opening of the cavity and V is the volume of the cavity. Comparing the results with these estimations, we find that the Helmholtz resonance of the cavity affects the vortex shedding at the cavity opening and that the oscillation mode n of the vortex shedding that is close to the resonant frequency of the cavity is selected, leading to the discontinuous change in frequency. In other words, the frequency of the pressure fluctuations is locked in at the Helmholtz resonant frequency of the cavity. The computational results capture this distinctive feature of fluid-resonant oscillation very successfully and agree well with the experimental data. The error is about 5%. The results using finer grids are in fair agreement with those using standard grids.

In Fig. 11, the distributions of the root mean square of non-dimensional pressure fluctuations in the plane of $z = 0$ are presented for four cases of incoming flow velocities. The interval of the contours is 0.05, and the bold line indicates that $Cp'_{\mathrm{rms}} \geq 0.2$. In the incompressible flow calculation, the pressure fluctuations appear only around the cavity opening where they are caused by unsteady vortex shedding. In contrast, the pressure fluctuations also appear in the cavity in the compressible flow calculation. The strong pressure fluctuations are especially apparent in the cases of $U_0 = 14$ and 34 m/s, where the amplitude of pressure fluctuation gives the local maximum value. These pressure fluctuations strongly suggest the occurrence of resonance. In comparison with these cases, the pressure fluctuation is weak in the case of $U_0 = 18$ m/s, where the amplitude of pressure fluctuation gives the local minimum value. In this case, the coupling between vortex shedding and resonance is considered to be weak. When the distributions are examined in detail, strong pressure fluctuations are found in the case of $U_0 = 34$ m/s at the back of the upstream edge of the cavity opening and in front of the downstream edge. In the case of $U_0 = 14$ m/s, strong pressure fluctuations are found also at the center of the opening. This difference is assumed to be the consequence of the oscillation mode change in vortex shedding because such a mode change would lead to a change in vortex wave length.

In Fig. 12, distributions of the instantaneous dilatation in the plane of $z = 0$ are presented for the case of $U_0 = 34$ m/s. As already mentioned, the additional term in Eq. (9), which expresses the weak compressibility effect, gives rise to the deviation from the divergence-free condition of the velocity vector. Thus, it is significant for the validation of the present method to examine whether the dilatation is estimated properly in the calculations. In Fig. 12, contours are plotted in the range from -0.01 to 0.01. The interval of the contours is 0.002. The thin line indicates a negative value, where the density is decreasing, and the bold line a positive value, where

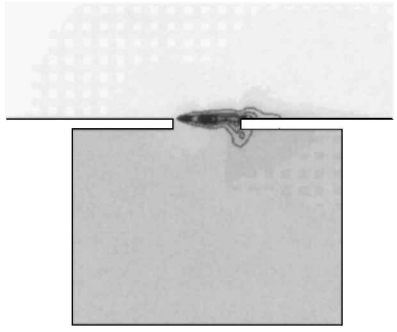

Incompressible flow calculation

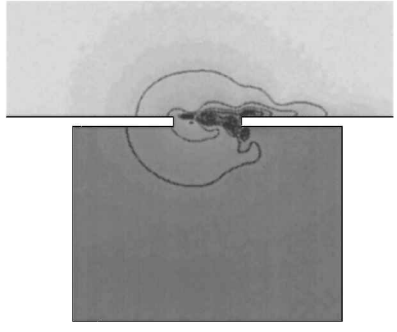

U_0 = 14 m/s

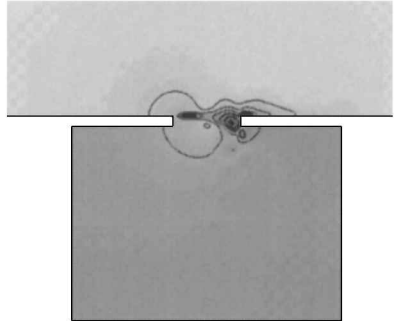

U_0 = 18 m/s

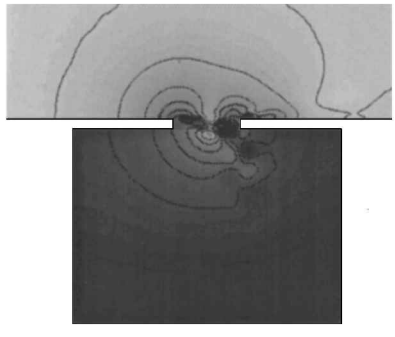

U_0 = 34 m/s

Fig. 11 Distributions of root mean square of nondimensional pressure fluctuations in z = 0 plane: Cp'_{rms} = 0 (white) ~ 0.5 (black).

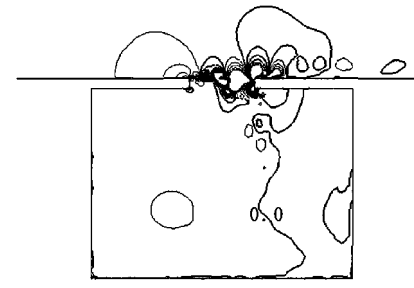

Time A

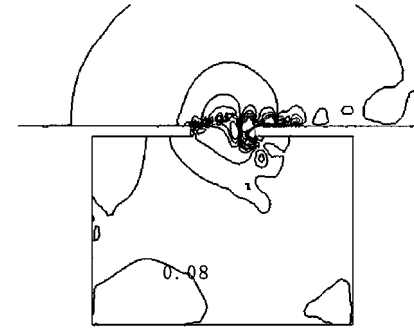

Time B

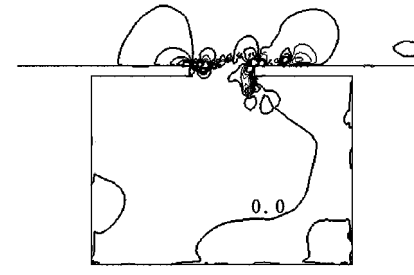

Time C

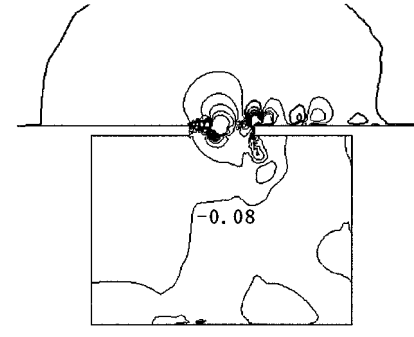

Time D

Fig. 12 Distributions of instantaneous dilatation (divergence of velocity vectors) in z = 0 plane, where the bold line is positive value and the thin line is negative value.

the density is increasing. The times A–D indicated in Fig. 8 are the typical phases in pressure fluctuation. It is seen that instantaneous dilatation is distributed continuously within and around the cavity. In the cavity, the velocity level is so low that the dilatation should be almost in proportion to $-\partial p/\partial t$ according to Eq. (9). At time A or C, when the pressure takes the maximum or minimum value and, thus, $\partial p/\partial t$ almost vanishes, the dilatation in the cavity becomes nearly zero. At time B, when the $\partial p/\partial t$ is negative, the dilatation in the cavity takes a positive value around 0.08, whereas at time D, when the $\partial p/\partial t$ is positive, the dilatation in the cavity takes a negative value around -0.08. These results confirm that the behavior of the dilatation is consistent with the pressure variation in the present calculation. Moreover, the residual for Eq. (9) in the present calculation is $\mathcal{O}(10^{-4})$ at most. This assures that the dilatation in the present calculation is not caused by numerical error. Thus, it is confirmed that the present result is the natural consequence of a properly estimated dilatation.

V. Conclusions

We derived a new equation set that is suited to predict numerically the fluid-resonant oscillation at low Mach numbers. The derived set of equations is essentially the same as the incompressible Navier–Stokes equations except for an additional term in the continuity equation that expresses the weak compressibility effect. The most important point for obtaining an accurate solution is to employ the numerical method that satisfies the continuity condition with high accuracy to capture the weak compressibility effect correctly. In this study, we modified the collocated grid system (confirmed to

satisfy the given requirement in the incompressible flow), making it applicable to the present equation set. Because the collocated grid system is one of the pressure-based methods that treat the continuity equation as a constraint equation for pressure, the stiffness problem that arises in solving the usual compressible flow equations under low-Mach-number conditions is also alleviated.

To examine the validity and the accuracy of the present method, we applied it to the numerical analysis of flows over a three-dimensional open cavity. The results show that strong pressure fluctuations occur at specific incoming flow-velocity conditions. We also demonstrate that the frequency of the pressure fluctuations is locked in at the Helmholtz resonant frequency of the cavity and that it varies discontinuously with the incoming flow velocity due to a change in the oscillation mode. All of these characteristics are distinctive features of fluid-resonant oscillation. Although we used a second-order spatial difference scheme, instead of the usually preferable higher-order differences schemes, and used an implicit method for the time advancement, we could predict the flow-velocity conditions that cause the peaks in the nondimensional pressure fluctuations and the frequency of the pressure fluctuations within an error of 5%. The maximum sound pressure level obtained by the calculation is about 5 dB lower than that obtained by the actual experiment, but the change in the amplitude of the pressure fluctuation with the incoming flow velocity agrees well overall with the experimental data. Thus, it is concluded that the present method is capable of predicting fluid-resonant oscillation in low-Mach-number flows.

References

[1]Rockwell, D., and Naudascher, E., "Review—Self-Sustaining Oscillations of Flow Past Cavities," *Journal of Fluids Engineering*, Vol. 100, June 1978, pp. 152–165.

[2]China, H., Kataoka, T., and Yoshida, M., "Simulation of Interface Oscillation Phenomenon over a Cavity in Air Flow," *Advances in Numerical Simulation of Turbulent Flows, Proceedings of the First Joint ASME-JSME Fluid Engineering Conference*, FED-119, American Society of Mechanical Engineers, 1991, pp. 71–76.

[3]Hardin, J. C., and Pope, D. S., "Sound Generation by Flow over a Two-Dimensional Cavity," *AIAA Journal*, Vol. 33, No. 3, 1995, pp. 407–412.

[4]Morinishi, Y., Lund, T. S., Vasilyev, O. V., and Moin, P., "Fully Conservative Higher Order Finite Difference Schemes for Incompressible Flow," *Journal of Computational Physics*, Vol. 143, No. 1, 1998, pp. 90–124.

[5]Rhie, C. M., and Chow, W. L., "Numerical Study of the Turbulent Flow Past an Airfoil with Trailing Edge Separation," *AIAA Journal*, Vol. 21, No. 11, 1983, pp. 1525–1532.

[6]Ferziger, J. H., "Simulation of Complex Turbulent Flows: Recent Advances and Prospects in Wind Engineering," *Journal of Wind Engineering*, No. 52, Supplement, 1992, pp. 1–19.

[7]Werner, H., and Wengle, H., "Large Eddy Simulation of Turbulent Flow over and Around a Cube in a Plate Channel," *Proceedings of the 8th Symposium on Turbulent Shear Flows*, 1991, pp. 19-4-1–19-4-6.

[8]Horinouchi, N., Kato, Y., Shinano, S., Kondoh, T., and Tagayashi, U., "Numerical Investigation of Vehicle Aerodynamics with Overlaid Grid System," Society of Automotive Engineers, SAE Paper 950628, 1995.

[9]Sarohia, V., "Experimental Investigation of Oscillations in Flows over Shallow Cavities," *AIAA Journal*, Vol. 15, No. 7, 1977, pp. 984–991.

[10]Gharib, M., "Response of the Cavity Shear Layer Oscillations to External Forcing," *AIAA Journal*, Vol. 25, No. 1, 1987, pp. 43–47.

[11]Rossiter, J. E., "Wind Tunnel Experiments on the Flow Over Rectangular Cavities at Subsonic and Transonic Speeds," Aeronautical Research Council, Reports and Memoranda 3438, London, 1966.

W. J. Devenport
Associate Editor